Analysis of Microscopic Anode Structure Effects on an Anode-Supported SOFC Including Knudsen Diffusion

Andersson, Martin; Lu, Xinrong; Yuan, Jinliang; Sundén, Bengt

Published in:
SOFC12

DOI:
10.1149/1.3570168

2011

Analysis of Microscopic Anode Structure Effects on an Anode-Supported SOFC Including Knudsen Diffusion

M. Andersson [a], X. Lu [b], J. Yuan [a], B. Sundén [a]

[a] Department of Energy Sciences, Lund University, SE-221 00 Lund, Sweden
[b] Marine Engineering College, Dalian Maritime University, Dalian 116026, China

In this study a two dimensional CFD (COMSOL Multiphysics) is employed to study the effect of anode microscopic structures on the transport phenomena and reactions for an anode-supported solid oxide fuel cell (SOFC). FCs can be considered as energy devices, involving multiple processes, such as (electro-) chemical reactions, heat exchange, gas- and ionic transport. All these complex processes are strongly integrated, needing modeling as an important tool to understand the couplings between mass-, heat-, momentum transport and chemical reactions. For the porous material, the Knudsen diffusion is taken into account in this study. The chemical- and electrochemical reaction rates depend on temperature, material structure, catalytic activity, degradation and partial pressure among others. It is found that the anode thickness and also the anode pore size need to be optimized to achieve high cell efficiency, when the Knudsen diffusion effects are included.

Introduction and Problem Statement

Fuel cells (FCs) produce electricity and heat directly from chemical conversion of fuel and oxidant energies by electrochemical reactions (1). The fuel cell is not a new invention, because the electrochemical process was discovered already in 1839. However the first real fuel cell system was not designed and built until the 1950s. The interest in fuel cells have been growing exponentially, concerning the number of scientific papers published after year 2000 (2). Among the various types of FCs, the solid oxide fuel cell (SOFC) has attained significant interests due to its high efficiency and low emissions of pollutants to the environment. High temperature operation offers many advantages, such as high electrochemical reaction rate, flexibility of using various fuels and tolerance to impurities. SOFC has in general either planar or tubular configurations (1-2), and its performance depends on thermal, (electro-) chemical and mechanical phenomena (3).

In an electrode-supported SOFC either the anode or cathode is relatively thick and works as support material. This design makes it possible to have a very thin electrolyte, i.e., the ion transfer losses decreases and the temperature can be lowered to 600-800 °C. Fuel cells working in this temperature range are classified as intermediate temperature (IT) (1) if compared to conventional (electrolyte-supported) SOFCs that operate between 800 and 1000 °C (4).

The global reactions that take place within a SOFC using a mixture of hydrogen, carbon monoxide and methane as fuel and oxygen in air as reductance can be described

as: oxygen is reduced in the cathode, Eq. 1. The oxygen ions are transported through the electrolyte, but the electrons are prevented to pass through the electrolyte. The electrochemical reactions, Eqs. 2-3, take place in the anodic three-phase boundary (TPB). Methane needs to be reformed, Eq. 4, before the electrochemical reactions. Carbon monoxide can be oxidized in the electrochemical reaction, Eq. 3, but can also react with water (Eq. 5) (5). The reactions described here are the overall ones, more detailed reaction mechanisms can be found in (6). Note that methane is not participating in the electrochemical reactions at the anodic TPB, it is catalytically converted within the anode, into carbon monoxide and hydrogen, which are used as fuel in the electrochemical reactions (5).

$$O_2 + 4e^- \Leftrightarrow 2O^{2-} \quad [1]$$

$$H_2 + O^{2-} \Leftrightarrow H_2O + 2e^- \quad [2]$$

$$CO + O^{2-} \Leftrightarrow CO_2 + 2e^- \quad [3]$$

$$CH_4 + H_2O \Leftrightarrow 3H_2 + CO \quad [4]$$

$$CO + H_2O \Leftrightarrow H_2 + CO_2 \quad [5]$$

Mathematical Model

A two-dimensional model for an anode-supported SOFC is developed and implemented in the commercial software, COMSOL Multiphysics (version 3.5). Equations for momentum-, mass- and heat transport are solved together with rate equations for internal reforming reactions. The geometry is defined in Table I and a sketch of the modeled cell can be seen in Fig 1. Note the difference in scale between the cell length (x-direction, as in Fig. 1) and various component thicknesses (y- direction, as in Fig. 1). It should be mentioned that the model in this study is 2D only, and the connection between the electrodes and interconnect can not be explicitly observed in this case.

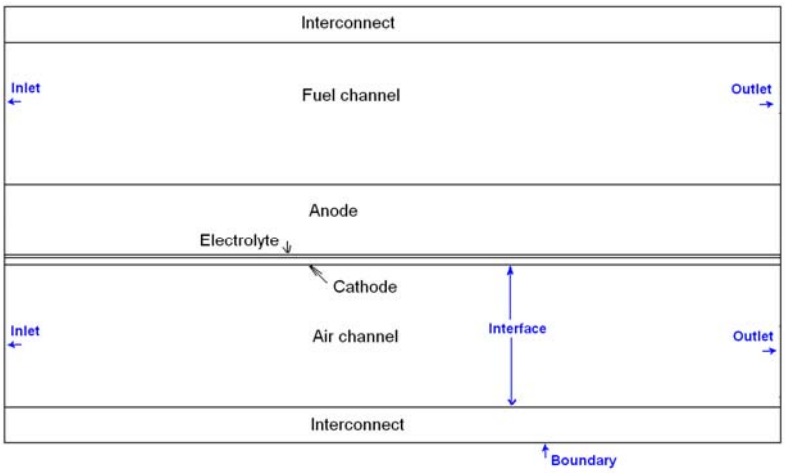

Figure 1. Sketch of an anode-supported SOFC, not to scale.

TABLE I. Cell geometry (7-8)

Cell Component	Thickness
Cell length	0.1 m
Fuel channel height	1 mm
Air channel height	1 mm
Anode thickness	500 μm
Cathode thickness	50 μm
Electrolyte thickness	20 μm
Interconnect thickness	500 μm

Momentum transport

The gases flow inside the fuel cell components, such as in the air and fuel channels, and in the porous electrodes. The Darcy-Brinkman equation is introduced and solved for the gas flow in the fuel and air channels, and in the porous materials simultaneously (9-10). The Darcy-Brinkman equation (Eq. 6) is transformed into the standard Navier-Stokes equation when $\kappa \to \infty$ and $\varepsilon_p = 1$, and into the Darcy equation as $Da \to 0$. Da is the Darcy number. The derivation of Navier-Stokes equation and Darcy equation from Darcy-Brinkman equation can be found in (9).

$$\left(\frac{\mu}{\kappa} + \rho \cdot \nabla \mathrm{u}\right)\mathrm{u} - \nabla\left[-p + \frac{1}{\varepsilon_p}\left\{\mathbf{T} - \left(\lambda - \kappa_{dv}\right)(\nabla \mathrm{u})\right\}\right] = \mathbf{F} \qquad [6]$$

where $\mathbf{F}$ is the volume force vector, κ is the permeability of the porous medium, ε_p the porosity, μ the dynamic viscosity, u the velocity vector and $\mathbf{T}$ the viscous stress tensor $\left(\mathbf{T} = \nu\left(\nabla \mathrm{u} + (\nabla \mathrm{u})^T\right)\right)$. λ is the second viscosity, and for gases it is normally assumed as: $\lambda = -2\mu/3$ (11). The densities and viscosities for the participating gases are dependent on local concentration and temperature, as described in (7-8). The gas inlet velocities are defined as a laminar flow profile. The outlets are defined as pressure (= 1 atm).

Mass transport

In the porous material, there are two kinds of mass diffusion mechanisms, i.e., molecular and Knudsen diffusions. The molecular diffusion is significant in the case of large pores, whose size is much bigger than the mean free path of the diffusion gas molecules (12-13). In this case, the intermolecular collisions will be dominated. For a multi-component gas mixture system, the diffusion coefficients are calculated by the expressions in (7-8).

Knudsen diffusion is important when the mean free path is much bigger than the pore size, and molecules collide with the solid walls more often than with other molecules**.** At the SOFC operating temperature of around 1000 K, the mean free path of these gas components is about 0.2-0.5 μm. In this study, the radius of pores is assumed as 0.34 μm, which is of the same order as the mean free path. In other words the Knudsen diffusion should be included in the SOFC models. The Knudsen diffusion coefficient of the component i with the component j in a gas mixture, $D_{k,ij}$, can be calculated based on the free molecule flow theory (14):

$$D_{k,ij} = \frac{2}{3} r_e \sqrt{\frac{8RT}{\pi(\frac{M_i + M_j}{2})^2}} \quad [7]$$

where r_e is the effective radius of the pore, R the universal gas constant. In the porous media, there is an increased diffusion length due to the tortuous paths of real pores, and the coefficients are usually corrected with porosity ε and tortuosity τ (13,14):

$$D_{eff,ij} = \frac{\varepsilon}{\tau} \cdot D = \frac{\varepsilon}{\tau} \cdot \left(\frac{D_{i,j} \cdot D_{k,ij}}{D_{i,j} + D_{k,ij}} \right) \quad [8]$$

Equation 9 is used to describe the mass transport phenomena for each gas component inside the cell (10) and solved for the fuel and air channels and the electrodes.

$$\nabla \left(-\rho \cdot w_i \sum^{n} \overline{D}_{eff,ij} \cdot \nabla x_j \left(x_j - w_j \right) \frac{\nabla p}{p} \cdot \mathrm{u} - D_i^T \cdot \frac{\nabla T}{T} \right) + \rho \cdot \mathrm{u} \cdot \nabla w_j = S_i \quad [9]$$

where w is the mass fraction, x the molar fraction, n the number of species and D_i^T the thermal diffusion coefficient. S_i, the source term by the chemical reactions, is only defined for the internal reforming reactions, because the electrochemical reactions are assumed to take place at the interfaces between the electrolyte and the electrodes. The ordinary diffusion coefficients are also dependent on the local temperature, as described in (7-8).

On the air side nitrogen and oxygen are involved and only one Maxwell-Stefan diffusion coefficient needs to be calculated. On the fuel side methane, water, hydrogen, carbon monoxide and carbon dioxide are present and 10 pairs of the Maxwell-Stefan diffusion coefficients need to be calculated and implemented in the model. The boundary conditions for the mass transport equation are defined as mass fraction for the gas channel inlets, the outlets are defined as convective flux.

Heat transport

The temperature distribution is calculated separately for the gas phase (in the air and fuel channels and the electrodes) and for the solid phase (the interconnects, the electrodes and the electrolyte). Heat is transferred between the phases at the channel walls and in the porous electrodes. The governing equations for the transport of heat are defined and explained in (7-8). The inlet gas temperature is defined by the operating temperature (1000 K) and the outlet one is defined as a convective flux. The boundaries at the top and the bottom of the cell are defined as symmetries, because it is assumed that the cell is surrounded by other ones with the same temperature distribution.

Electrochemical reactions

Two approaches for defining the electrochemical reactions can be found in the literature, either as source terms in the governing equations (14-15) or as interface conditions defined at the electrode/electrolyte interfaces (16-17). The later approach is

employed in this study, because the thickness of the active layer is sufficiently thin, compared to the thickness of the electrode (16-17). The charge transfer equations are not solved in this study, however effects of the ohmic-, the concentration- and the activation polarization losses are included in the governing equations for heat transport by interface or source terms. The equations for polarization losses and exchange current density are described in (7-8).

Both hydrogen and carbon monoxide can participate in electrochemical reactions with oxygen ions (Eqs. 2-3). The electrochemical oxidation of hydrogen is several times higher than that of carbon monoxide, while the water-gas shift reaction is relatively fast (14). The contribution of oxidation of carbon monoxide has been neglected in this study. The cell average current density is specified to 0.3 A/cm^2 in this study.

Internal reforming reactions

Sufficient activity for the reforming reactions is provided inside the SOFC anode (18). Reaction kinetics from (19) for the steam reforming (an expression dependent on the active area to volume ratio) and from (20) for the water-gas shift reactions are used to calculate the reaction rates in this work. Other global kinetic models can be found in (21-22). The catalytic steam reforming reaction occurs at the surfaces of the nickel catalysts and is specified as (19,23):

$$r_r = AV \cdot \left(943 \cdot \exp\left(\frac{-225 \cdot 10^3}{R \cdot T} \right) \cdot p_{CH_4} p_{H_2O} - 7.74 \cdot 10^{-9} \cdot \exp\left(\frac{-1937}{R \cdot T} \right) \cdot p_{CO} p_{H_2}^3 \right) \qquad [10]$$

where p_i is the partial pressure of gas species i, T the temperature, r the reaction rate and AV the active surface area to volume ratio. Equation 10 origins from the experiments performed at Research Centre Jülish, and the anode material consists of Ni−8YSZ substrate with a standard composition of 50 wt% Ni (23).

The range for the AV (related to catalytic kinetic reactions) varies in the literature between $1 \cdot 10^5$ m^2/m^3 (24) and $2.2 \cdot 10^6$ m^2/m^3 (19) for SOFC anodes. The measured specific surface area (m^2/g) for Ni/YSZ material developed for SOFC anodes is $70 \cdot 10^6$ m^2/m^3 (25). Note that not all the surfaces are available for catalytic reactions, due to the distribution of catalyst, non available pores and mass transfer limitations among others. An AV of $2.2 \cdot 10^6$ m^2/m^3, corresponding to 3.1 percent of the total Ni/YSZ specific area to volume ratio, is used in this work. The trend for the development during the last years is in the direction of employing smaller pores to get a larger AV.

The reaction rate, eq. 10, is of the Arrhenius type. It consists of three parts, partial pressures, pre-exponential factor and activation energy. The pre-exponential factor describes the amount of collisions between the molecules within the reaction and the exponential expression with the activation energy describes the probability for the reaction to occur. The pre-exponential factors depend strongly on the properties of the anode material and the temperature. The activation energy is based on the catalytic characteristics, such as chemical composition. The large difference between the activation energies in the open literature (19, 21-23) makes it probable that more parameters have significant influences on the reaction rate. To truly enhance the understanding of these

phenomena microscale modeling involving microscopic feature of the porous structures is needed.

Different approaches for defining the water-gas shift reaction can be found in literature: **1.** Global reaction mechanism that considers reaction in the anode only (5,14,20). **2.** Global reaction mechanism that considers reaction in the anode and in the fuel channel (4,19). **3.** A more advanced reaction mechanism that includes catalytic surface reaction kinetics for integrated steam reforming, water-gas shift reaction and the Boudouard mechanism can be found in, e.g., (4,6). Based on the global scheme for the anode, the expression for the catalyzed water-gas shift reaction in (20) has been selected in this study:

$$r_s = k_{sf} \cdot \left(p_{H_2O} p_{CO} - \frac{p_{H_2} p_{CO_2}}{K_{ps}} \right) \qquad [11]$$

The rate constant (k_{sf}) and the equilibrium constant (K_{ps}) are temperature dependent expressions calculated from experimental data, as described in (20).

The source terms S_i (implemented in the Maxwell-Stefan equations for the gas species), due to the catalytical reforming reactions and the heat generation/consumption due to the reforming reactions is specified in (7-8).

Results and Discussion

The fuel gas inlet conditions are specified as $x_{H2} : x_{CH4} : x_{CO} : x_{H2O} : x_{CO2} = 0.2626 : 0.171 : 0.0294 : 0.4934 : 0.0436$ (defined by IEA as 30% pre-reformed natural gas) (7-8), and the gas inlet temperature is specified as 1000 K. An average cell current density is 0.3 A/cm^2, an oxygen consumption is 20 % (mole), fuel consumption 80 % (mole), and flow direction from left -> right for both the anode and the fuel channels are defined. Typical SOFC material characteristic data used in this work are found in (7-8). The pore radius is for the standard case defined as 0.34 μm and the ratio of the anode thickness to the anode height to 33%.

Parameter studies are also performed for the anode pore size and the anode thickness ratios. The anode thickness ratio is defined as:

$$th_{anode}(\%) = \frac{d_{anode}}{d_{anode} + d_{fuelchannel}} \qquad [12]$$

The anode thickness ratio is 33% for the standard case, and 25% and 40% for the parameter studies. Note that the fuel channel height is kept constant for all the investigated cases.

As predicted, the temperature increases along the x-direction (the main flow direction), as seen in Fig. 2a. The heat generation is due to the electrochemical reactions and related over-potential losses. The methane steam reforming (MSR) consumes heat, up to half of the heat generated. The temperature difference in the y-direction inside the air channel

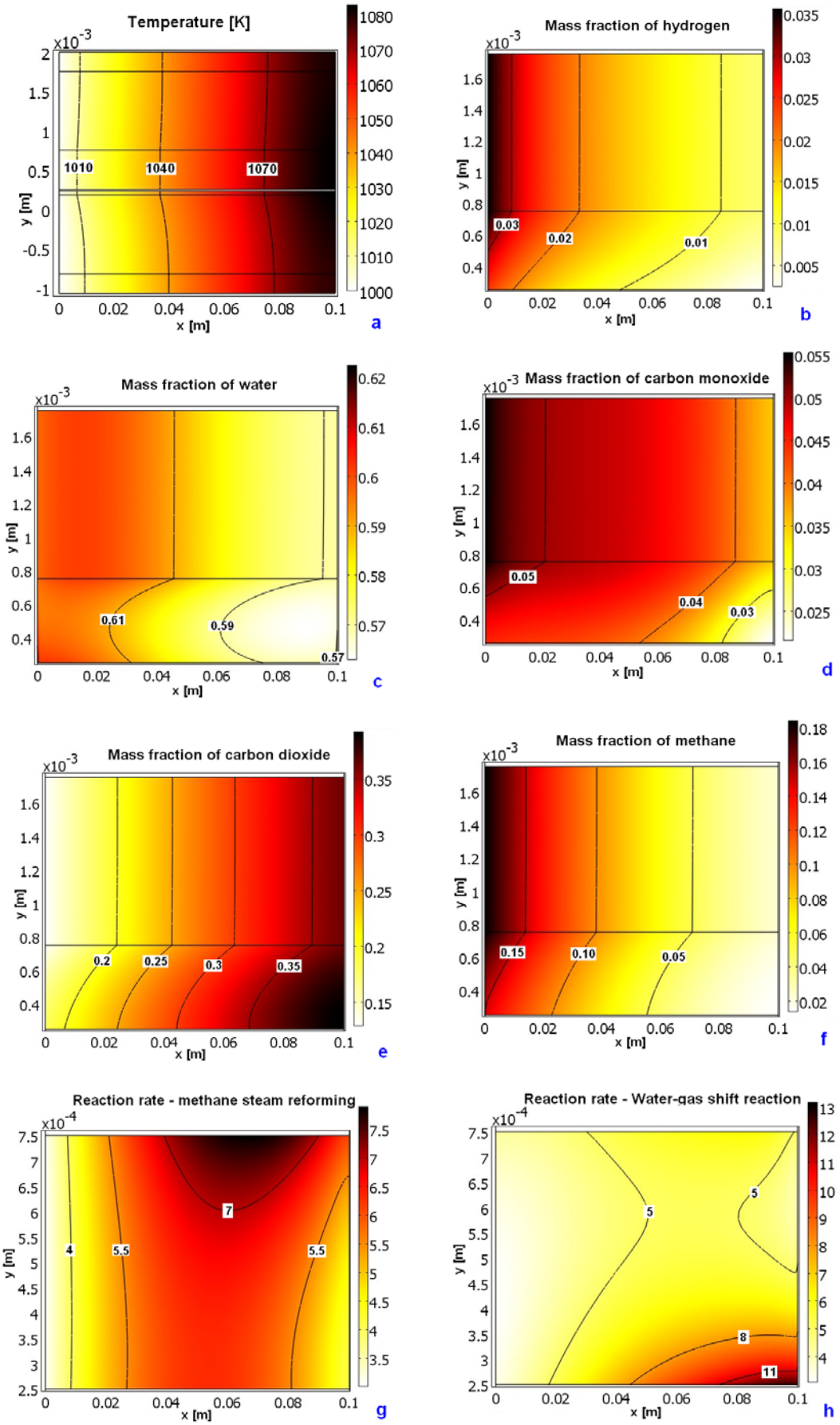

Figure 2. Temperature (a), mass fractions (b-f) and reaction rates (g-h) for the basic case.

occurs because the convective heat flux are bigger in the air channel (compared to the fuel channel) due to the relatively larger air flow rate. No significant difference for the temperature distribution can be seen when this model is compared to our previous developed model (7) with neglected Knudsen diffusion. Note the different scale in the x and y direction. For temperature distribution and mass fraction distributions the fuel channel (top) and anode (bottom) are presented, while for the reaction rate only the anode is shown.

The mass fraction of hydrogen (Fig. 2b) decreases due to the electrochemical reactions at the anode/electrolyte interface and increases due to the reforming reactions. The effect of Knudsen diffusion is significant. Large concentration gradients can be observed through the cell (y-direction) and the amount of hydrogen available for electrochemical reactions, at the TPB, is reduced, compared to our model with neglected Knudsen diffusion (7). Water (Fig. 2c) is generated due to the electrochemical reactions and consumed in the reforming reactions. The concentration of water reaches to its lowest value in the middle of the anode (y-direction). This effect can not be observed in our previously developed model, with neglected Knudsen diffusion (7). Carbon monoxide (Fig. 2d) is generated in the MSR and consumed in the water-gas shift reaction (WGSR). The concentration gradient through the anode is, due to the Knudsen diffusion effect, large and the smallest concentration is found at the TPB. Carbon dioxide (Fig. 2e) is generated in the WGSR and transported through the anode and out of the cell with the exhaust flow stream. A distinct concentration gradient can be seen through the anode (y-direction), due to the Knudsen diffusion effect. The highest concentration is found close to the gas outlet at the TPB. Methane (Fig. 2f) is consumed in the MSR. Also for methane a clear concentration gradient is seen through the anode, due to the Knudsen diffusion effect. The lowest concentration is found at the TPB close to the gas outlet.

The MSR (Fig. 1g) reaction rate depends on the available active area, temperature, and concentration of methane and water within the anode. It increases as the temperature increases along the flow direction and decreases as the amount of methane is reduced. In our previously developed model (7), with no Knudsen diffusion effect, only very small differences in reaction rate through the anode can be observed, however in this model the reaction rate is higher close to the fuel channel and lower closer to the TPB. The WGSR reaction rate (Fig. 2h) reaches its highest value close to the anode/electrolyte interface. As hydrogen is consumed and steam generated due to electrochemical reaction the water-gas shift reaction proceeds to the right and more hydrogen is generated. Our model (7), where Knudsen diffusion is neglected, predicted large concentration gradients within the anode (x-direction) close to the inlet. This effect does not appear in this model, due to larger diffusion resistance. It should be mentioned that the forward and backward reaction rates are in the same magnitude for the WGSR, to be compared to the MSR, where the backward reaction is neglible.

The anode pore size is varied to investigate the effects on transport processes, in terms of the hydrogen mass fraction distribution (Fig. 3a-b). These plots should be compared to Fig. 1b, where the mass fraction distribution for the standard case (r=0.34μm) is shown. An increased pore size means decreased mass transfer resistance but also a decreased surface area. Decreased mass transfer resistance gives a less steep concentration change in the y-direction in the anode. A decreased surface area results in a decreased MSR, i.e., the hydrogen concentration in the exhaust gas decreases.

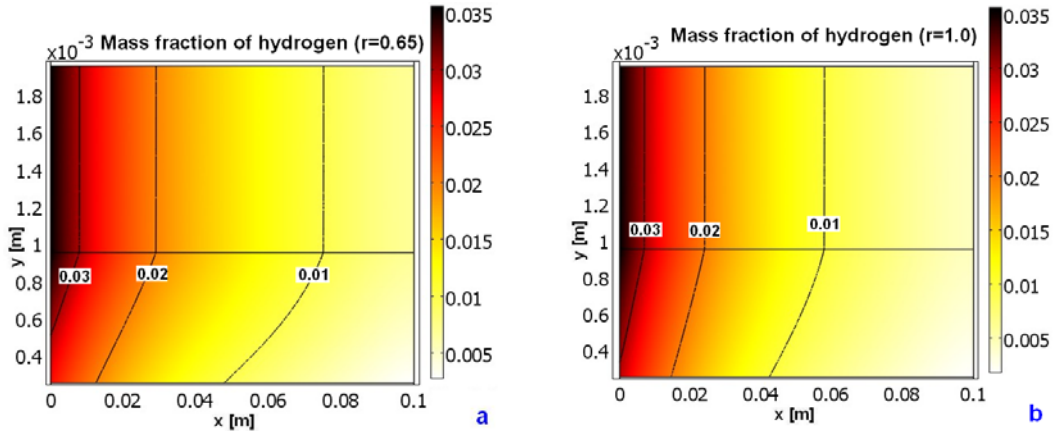

Figure 3. Mass fraction of hydrogen as the anode pore size is increased for the fuel channel (up) and anode.

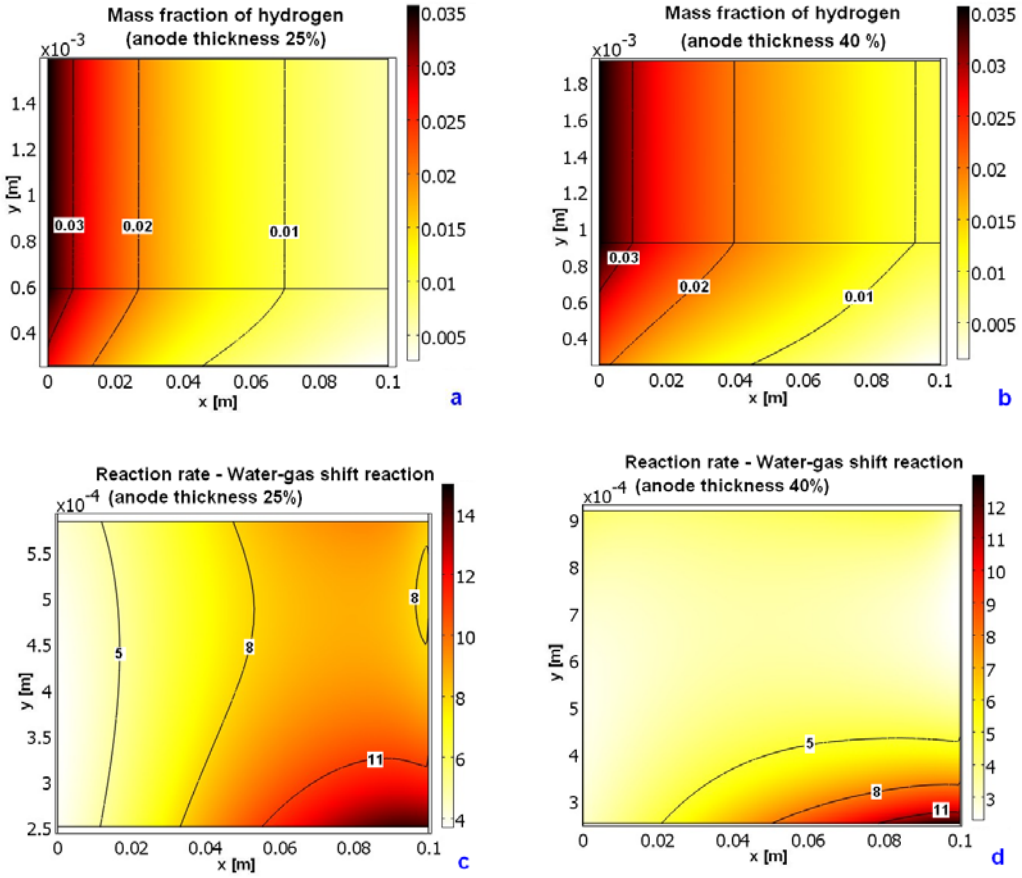

Figure 4. Mass fraction of hydrogen (a-b) for the fuel channel (top) and anode (bottom) and water-gas shift reaction rate (c-d) within the anode, affected by anode thickness.

The anode thickness is varied to investigate the consequences on the hydrogen mass fraction distribution (Fig. 4 a-b) and also WGSR reaction rate (Fig. 4 c-d). Comparisons are made to Fig. 1 b and h, respectively, where the standard case is revealed. A thicker anode (40%) gives higher mass fraction of hydrogen at the fuel channel/anode interface, but the large diffusion resistance (due to the longer diffusion length within the anode)

gives a low value at the anode/electrolyte interface and also a large concentration change in the y-direction. A thinner anode (25%) makes the smaller diffusion resistance between the fuel channel and anode/electrolyte interface, however the active surface area available for MSR is also reduced. Only a portion of the anode is used for the most WGSR in the case of a thicker anode, compared to the case with a thinner anode, where the reaction is distributed over a major part of the anode, as shown in Figs. 4a and 4c.

Conclusion

A CFD approach is developed and implemented to analyze physical and chemical phenomena, which take place inside a single anode-supported SOFC by including Knudsen diffusion effects. Equations for mass-, heat- and momentum transport are coupled to the internal reforming reactions. The heat, which is generated due to the electrochemical reactions, is used for internal steam reforming reaction within the anode and/or outside the cell for external reforming and pre-heating of the fuel and air.

From the above analysis, there is an obvious change of concentration distributions in the anode, it means that there are extra resistances in the porous material because the size of pores is at the same order of the magnitude as the mean free path, i.e., the Knudsen diffusion plays an important role. Taking Knudsen diffusion into account is reasonable and necessary.

It is concluded that the pore size and the anode thickness need to be optimized to achieve good performance and a high efficiency particularly when the Knudsen diffusion is included. Thinner anodes reduces the diffusion length and resistance, however the active surface area for methane steam reforming is simultaneously reduced. Smaller anode pore size increases the active surface area, however the diffusion resistance through the anode is increased. It should be mentioned that the operating temperature may be optimized to compensate these effects of various changes from cell design and configuration parameters.

Acknowledgments

The financial support from the Swedish Research Council (VR) and the European Research Council (ERC) is gratefully acknowledged.

References

1. Y. Patcharavorachot, A. Arpornwichanop, A. Chuachuebsuk, *J. Power Sources*, **177**, 254-261 (2008).
2. M. Saxe, Doctoral thesis, KTH, Sweden (2008).
3. K. Reifsnider, X. Huang, G. Ju, R. Solasi, *J. Mater. Sci.*, **41**, 6751-6759 (2006).
4. P. Aguiar, C.S. Adjiman and N.P. Brandon, *J. Power Sources,* **138**, 120-136 (2004).
5. M. Ni, M.K.H. Leung, D.Y.C., *J. Power Sources*, **168,** 369-378 (2007).
6. V. Janardhanan, O. Deutschmann, *J. Power Sources*, **162**, 1192-1202 (2006).
7. M. Andersson, SOFC Modeling Considering Mass and Heat Transfer, Fluid Flow with Internal Reforming Reactions, Licentiate Thesis, Department of Energy Sciences, Lund University, Sweden, (2009).

8. M. Andersson, H. Paradis, J. Yuan, B. Sundén, *J. Fuel Cells* (2010, in press).
9. M. Le Bars, M.G. Worster, 2006, *J. Fluid Mech.*, **550**, 149-173 (2006).
10. COMSOL Multiphysics 3.5 user guide, Stockholm, Sweden (2008).
11. H.K. Versteeg, W. Malalasekera, An Introduction to Computational Fluid Dynamics, The Finite Volume Method, Pearson, UK (1995).
12. S. Yixiang, C. Ningsheng, C. Li, *J. Power Sources,* **164**, 639-648 (2007).
13. D. Y. Murzin, T. Salmi, Catalytic Kinetics, Elsevier Science (2005).
14. J. Yuan, Y. Huang, B. Sundén, W. Wang, *Heat Mass Transfer,* **45**, 471-484 (2009).
15. M. Hussein, X. Li, I. Dincer, *Int. J. Thermal Sciences*, **46**, 48-86 (2007).
16. R. Suwanwarangkul, E. Croiset, M.W. Fowler, P.L. Douglas, E. Entchev, M.A. Douglas, *J. Power Sources*, **122**, 9-18 (2003).
17. K. Tseronis, I.K. Kookos, C. Theodoropoulos, *Chem. Eng. Sci.*, **63**, 5626-5638 (2006).
18. J.R. Ferguson, J.M. Fiard, R. Herbin, *J. Power Sources,* **58**, 109-122 (1996).
19. J.-M. Klein, Y. Bultel, S. Georges, M. Pons, *Chem. Eng. Sci.*, **62**, 1636-1649 (2007).
20. B.A. Haberman, J.B. Young, *Int. J. Heat and Mass Transfer*, **47**, 3617-3629 (2004).
21. F. Nagel, T. Schildhauer, S. Biollaz, S. Stucki, *J. Power Sources*, **184**, 129-142 (2008).
22. D. Sanchez, R. Chacartegui, A. Munoz, T. Sanchez, *Int. J. Hydrogen Energy*, **33**, 1834-1844 (2008).
23. I. Drescher, W. Lehnert, J. Meusinger, *Electrochimica Acta,* **43**, 3059-3068 (1998).
24. V. Danilov, M. Tade, *Int. J. Hydrogen Energy*, **34**, 8998-9006 (2009).
25. D. Marrero-López, J.C. Ruiz-Morales, J. Peña-Martínez, J. Canales-Vázquez, P. Núñez, *J. Solid State Chemistry*, **181**, 685-692 (2008).